

1 **Distinct sources of interannual subtropical and subpolar**

2 **Atlantic overturning variability**

3 Yavor Kostov¹, Helen L. Johnson², David P. Marshall³

4 Patrick Heimbach^{4,5,6}, Gael Forget⁷, N. Penny Holliday⁸, M. Susan Lozier⁹,

5 Feili Li⁹, Helen R. Pillar⁴, Timothy Smith⁴

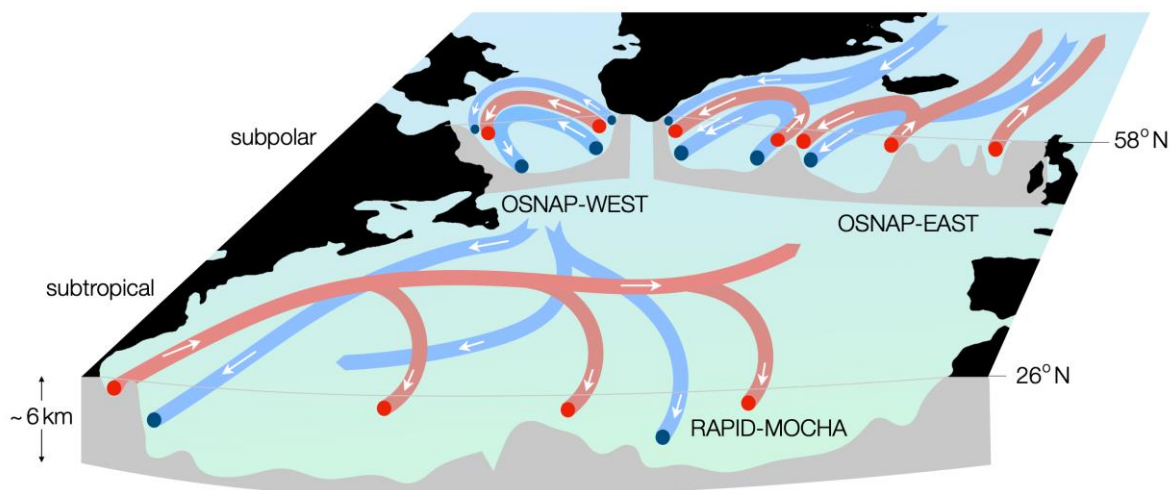
- 6 1. University of Exeter, Geography, Exeter, United Kingdom of Great Britain and
7 Northern Ireland (y.kostov@exeter.ac.uk)
- 8 2. University of Oxford, Earth Sciences, Oxford, United Kingdom of Great Britain and Northern Ireland
- 9 3. University of Oxford, Physics, Oxford, United Kingdom of Great Britain and Northern Ireland
- 10 4. University of Texas at Austin, Oden Institute for Computational Engineering and
11 Sciences, Austin, Texas, United States of America
- 12 5. Jackson School of Geosciences, University of Texas at Austin, Austin, TX, USA
- 13 6. Institute for Geophysics, University of Texas at Austin, Austin, TX, USA
- 14 7. Massachusetts Institute of Technology, Earth, Atmospheric, and Planetary Sciences,
15 Cambridge, Massachusetts, United States of America
- 16 8. National Oceanography Centre, Southampton, United Kingdom of Great Britain and
17 Northern Ireland
- 18 9. Georgia Institute of Technology, Earth and Atmospheric Sciences, Atlanta, Georgia
19 United States of America

20 **The Atlantic meridional overturning circulation (AMOC) is pivotal for regional and**
21 **global climate due to its key role in the uptake and redistribution of heat and carbon.**
22 **Establishing the causes of historical variability in AMOC strength on different timescales**
23 **can tell us how the circulation may respond to natural and anthropogenic changes at the**
24 **ocean surface. However, understanding observed AMOC variability is challenging**
25 **because the circulation is influenced by multiple factors that co-vary and whose**
26 **overlapping impacts persist for years. Here we reconstruct and unambiguously attribute**
27 **intermonthly and interannual AMOC variability at two observational arrays to the**

28 **recent history of surface wind stress, temperature and salinity. We use a state-of-the-art**
29 **technique that computes space- and time-varying sensitivity patterns of the AMOC**
30 **strength with respect to multiple surface properties from a numerical ocean circulation**
31 **model constrained by observations. While, on interannual timescales, AMOC variability**
32 **at 26° N is overwhelmingly dominated by a linear response to local wind stress,**
33 **overturning variability at subpolar latitudes is generated by the combined effects of wind**
34 **stress and surface buoyancy anomalies. Our analysis provides a quantitative attribution**
35 **of subpolar AMOC variability to temperature, salinity and wind anomalies at the ocean**
36 **surface.**

37

38 Throughout the upper kilometer, the Atlantic meridional overturning circulation (AMOC)
39 carries warm, high-salinity waters northward, while at depth it transports colder, low-salinity
40 waters southward in a zonal mean sense (1). Coupled climate models suggest that the AMOC
41 is likely to weaken over the coming decades, resulting in a decrease in the associated northward
42 heat transport, with widespread implications for regional and global climate (2). Continuous
43 observations of the AMOC since 2004 at 26°N, the location of the RAPID-MOCHA array, and
44 since 2014 at subpolar latitudes, where the OSNAP array has been deployed, reveal large
45 amplitude variability on all timescales accessible to date (3,4,5). Disentangling the roles of
46 anomalies in wind stress and sea-surface temperature and salinity (SST and SSS) in driving
47 historical AMOC variability has been a major obstacle, limiting our understanding of past
48 changes and our ability to critically assess model predictions of the future of the overturning
49 circulation. The fact that SST and SSS themselves respond to changes in the ocean circulation,
50 which can be independent of local atmospheric forcing, makes distinguishing cause and effect
51 even more challenging.



52

53 **Figure 1. Schematic of the large-scale ocean circulation in the subtropical and**
 54 **subpolar North Atlantic.** Colors differentiate major (red) warm, saline; and (blue) cool,
 55 fresh pathways of ocean currents. Bathymetric cross sections are shown in gray at the
 56 locations of the OSNAP-WEST, OSNAP-EAST, and RAPID-MOCHA arrays.

57 Attributing AMOC variability has traditionally been approached through perturbation
 58 experiments in climate models (6, 7). However, a prohibitively large number of perturbation
 59 simulations is necessary in order to fully resolve the spatially and seasonally-varying
 60 sensitivity of the AMOC to surface boundary conditions. Another standard method in
 61 attribution studies involves statistical analysis of the co-variability between the overturning
 62 circulation and surface properties such as air-sea heat flux, SST, SSS, and wind stress (7, 8).
 63 Still, many observables in the climate system co-vary and correlations among them do not
 64 reveal the direction of causality. Here we take a different approach towards attribution and use
 65 the adjoint (9,10) of an ocean model to establish unambiguous causal relationships (11, 12)
 66 between quantities at the air-sea interface and the lagged response of the AMOC. The adjoint
 67 of an ocean circulation model allows us to compute the sensitivity of a chosen metric, here the
 68 AMOC at a given latitude, to a range of variables, parameter choices, initial conditions and
 69 boundary conditions at various lead times (10, 11, 12). We use algorithmic differentiation (13)

70 to generate the adjoint (see Methods) of the ECCO version 4 (hereafter ECCO) configuration
 71 (10, 14) of the MITgcm, a state-of-the art ocean general circulation model (15). ECCO is an ocean state
 72 estimate, a data assimilation product in which a model simulation has been fit to historical observations in
 73 a least-squares sense so as to best represent the evolution of ocean properties over the period 1992-2015
 74 (10, 14, 16, 17). ECCO skillfully reproduces measurements of temperature and salinity (10, 14, 16, 17, 18),
 75 as well as the overturning circulation in the North Atlantic (See Figure S1 in the SI).

76 Here we use this advanced computational framework to produce a quantitative attribution
 77 of AMOC variability in the subpolar North Atlantic to anomalies in SST, SSS, and surface wind
 78 stress at different lead times. We focus on OSNAP-EAST rather than OSNAP-WEST (Figure 1)
 79 because the observed mean transport and variability in the Eastern Subpolar North Atlantic is greater and
 80 is known to play an important role in the large-scale transformation from lighter into denser water masses
 81 (19, 20, 21). We consider inter-monthly and inter-annual timescales and contrast the response of the
 82 subpolar AMOC against that of the overturning across the RAPID-MOCHA mooring array at 26°N.

83 *Reconstruction of the OSNAP-EAST and RAPID-MOCHA AMOC*

84 We use the adjoint of the MITgcm ECCO configuration to isolate the sensitivity of the
 85 overturning circulation to wind stress from its sensitivity to SST and SSS. This separation is critical
 86 because changes in wind can lead to substantial anomalies in ocean temperature and salinity. We
 87 then convolve these sensitivity patterns ($\mathcal{G}_{\mathcal{P}}$), which depend on the season, with surface wind
 88 stress, SST, and SSS anomalies between 1992 and 2015 from the ECCO state estimate. Each
 89 convolution provides an estimate for the time-evolving contribution C of the anomaly in a
 90 particular ocean surface property \mathcal{P} (temperature, salinity, or wind stress) to historical variability
 91 in the rate of meridional overturning (the volume transport in Sverdrups, where 1 Sv = 10^6 m³s⁻¹):

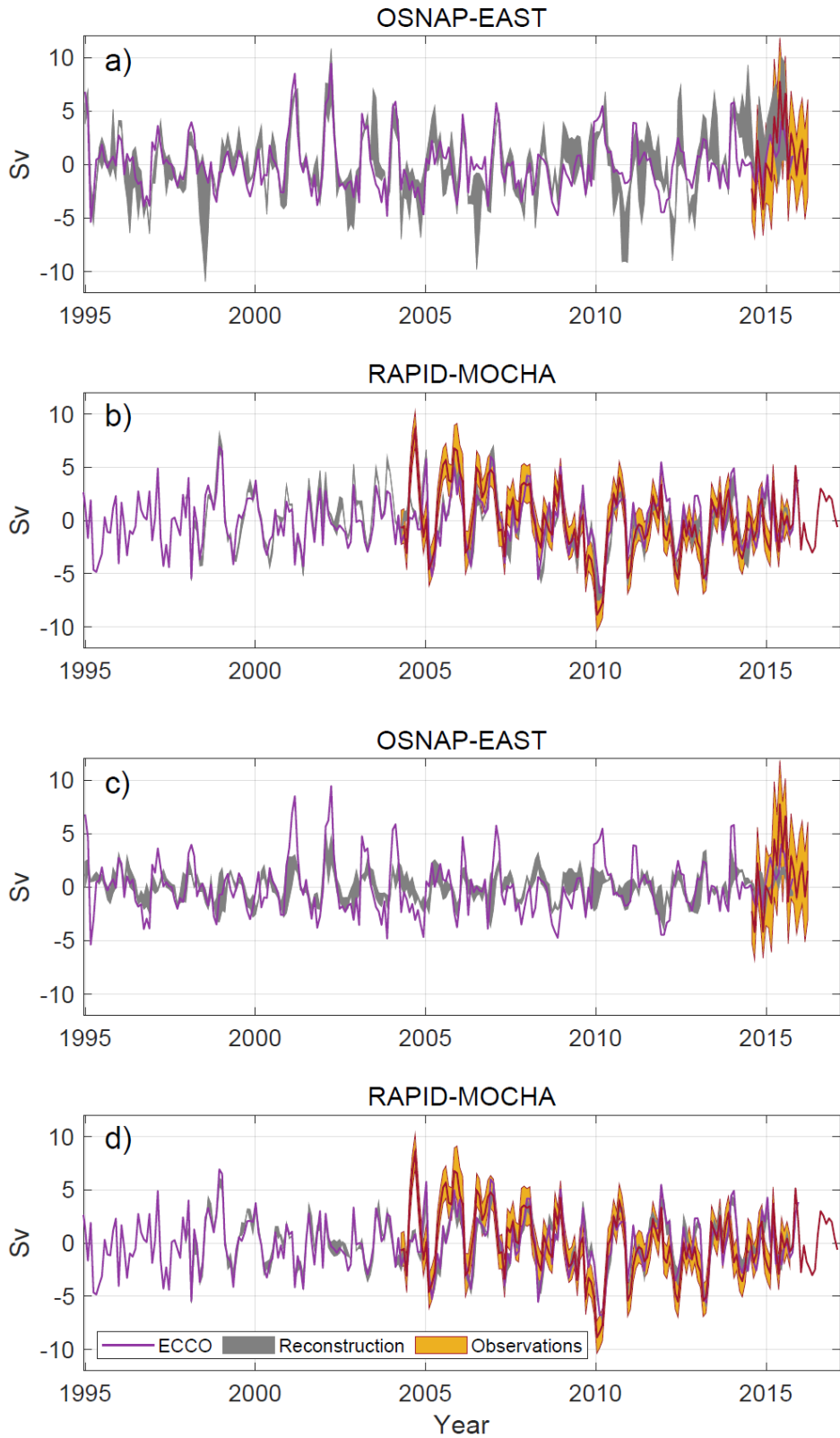
$$92 \quad C_{\mathcal{P}}(t) = \int_{t-\tau}^t \int \mathcal{P}(\mathbf{x}, t') \mathcal{G}_{\mathcal{P}}(t; \mathbf{x}, t - t') d\mathbf{x} dt', \quad (1)$$

93 where \mathcal{P} is the surface property anomaly relative to the climatology at a lead time t' , up to a
94 memory τ , and location \mathbf{x} ; see Methods for further details. We sum the contributions from SST,
95 SSS, and wind stress anomalies relative to the seasonal mean and then add the climatological
96 seasonal cycle in overturning (11) from the ECCO state estimate. We thus reconstruct AMOC
97 variability relative to the long-term mean at the latitudes of both the OSNAP-EAST and the
98 RAPID-MOCHA arrays. We separately consider how individual sources of variability
99 contribute to the total reconstruction. Furthermore, we explore how the seasonality in wind
100 stress contributes to variability in the overturning relative to the long-term mean.

101 The reconstructed overturning variability across OSNAP-EAST (Figure 2a) is significantly
102 correlated ($R=0.69$, and $R=0.72$ if we detrend the timeseries) with the historical overturning as represented in
103 ECCO. The reconstruction of overturning variability at the latitude of the RAPID-MOCHA array (Figure
104 2b), based on surface wind stress, SST, and SSS, also shows good agreement with the ECCO state estimate
105 ($R=0.89$) and with the direct observational estimate ($R=0.70$). Our reconstruction reproduces skillfully the
106 sign, magnitude, and timing of the AMOC anomalies (Figure 2a,b). This high level of agreement suggests
107 that AMOC variability is dominated by processes and mechanisms that our analysis largely captures.

108 The OSNAP-EAST observational record of 21 months is much shorter than that in the
109 subtropical Atlantic, but first indications suggest that our reconstruction also captures some of
110 the observed AMOC variability here. We interpolate our OSNAP-EAST reconstruction onto
111 the same 30-day time windows as the direct observational estimate (See Extended Data Figure
112 ED1). In 14 out of the 15 time windows where OSNAP-EAST observations and model output
113 are both available, our envelope of reconstructions overlaps with the direct observational
114 estimate within one standard error (See Extended Data Figure ED1). However, over this short
115 record, inter-monthly variability in our reconstructed OSNAP-EAST overturning is not
116 positively nor significantly correlated with the observational time series.

117



120 **Figure 2. Reconstruction of overturning in the North Atlantic.** Linear
 121 reconstruction (gray) of variability in OSNAP-EAST (a,c) and RAPID-MOCHA (b,d)

122 meridional overturning (volume transport in Sv) compared with the ECCO state
123 estimate (purple) and the direct observational estimate (yellow and brown). Anomalies
124 are shown relative to the long-term mean. The yellow shaded envelopes indicate ± 1
125 standard deviation of the observational uncertainty at OSNAP-EAST (see 19) and
126 RAPID-MOCHA (See 35), and the thick brown lines show the mean estimates. The
127 uncertainty of the observed RAPID-MOCHA overturning is not available for the last 17
128 months of the timeseries (the thick brown line in b and d). The reconstructions in a
129 and b include contributions due to surface wind stress, SST, SSS, as well as the
130 climatological seasonal cycle in overturning from ECCO. The thickness of the gray
131 shading in a,b indicates the spread between two estimates of the reconstructed AMOC
132 in ECCO, reflecting variability in the reference state about which the linearized
133 reconstruction is computed (see Methods). The reconstructions in c,d show only
134 contributions due to surface wind stress anomalies – including the contribution from
135 the seasonal cycle in winds – under fixed SST and SSS.

136 Nonlinearity in the sensitivity of the overturning circulation to surface forcing such as
137 SST and SSS is a key potential source of uncertainty in our reconstructions. An important
138 manifestation of nonlinearity in the overturning is the dependence of the sensitivity patterns,
139 and hence the AMOC reconstructions, on the evolving background state of the ocean. For
140 example, the exact sites of intense winter convection and deep water formation in the North
141 Atlantic differ from one year to another. The gray shaded envelopes in Figure 2a,b show the
142 spread in reconstructed AMOC variability that results from using sensitivity patterns computed
143 over two different historical periods in ECCO: one ending in 2001-2002 and one in 2006-2007.
144 (see Methods). This largely reflects changes in the sensitivity to wintertime surface buoyancy
145 anomalies between the two periods analyzed. This can be seen by comparing the large spread

146 in the full reconstruction that includes the buoyancy component (Fig 2a) to the diminished spread in
147 the wind-only reconstruction (Fig 2c). The dependence on the background state is more pronounced
148 in the OSNAP-EAST timeseries than the subtropical RAPID-MOCHA AMOC and explains the
149 lower skill in recovering the subpolar overturning. In addition, for numerical reasons, the adjoint of
150 the model approximates the parameterization of vertical mixing and sea ice physics, nonlinear
151 processes that are very active in the high latitude oceans and thus affect more strongly the OSNAP-
152 EAST reconstruction compared to the RAPID-MOCHA AMOC.

153

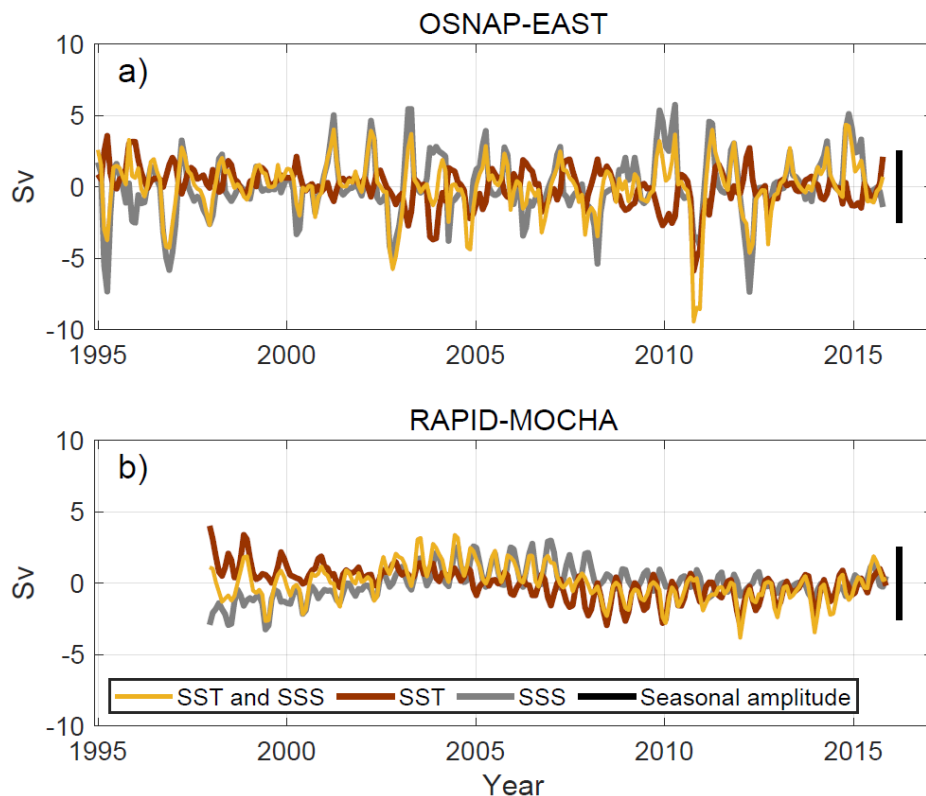
154 *Attribution of AMOC variability to wind, SST, and SSS*

155 Much of the variability ($R=0.94$) in historical overturning at 26°N can be explained in terms of wind-
156 driven circulation anomalies (Figure 2d and 4a,b; 11). A large fraction of the inter-monthly AMOC
157 anomalies at the RAPID-MOCHA array is attributed to processes within the surface Ekman boundary
158 layer ($R=0.70$, Extended Data Figure ED2), where there is a local balance between wind stress and a
159 component of the Coriolis force (22). Surface buoyancy anomalies contribute to low-frequency
160 variability in the subtropical AMOC, such as the reconstructed 2007-2011 decline in the overturning
161 at the RAPID-MOCHA array (Figure 3b). This historical weakening of the AMOC is very
162 pronounced in the observational time-series (4; Figure 2b) but less so in ECCO (Figure 2b), possibly
163 because high latitude density variability in the state estimate is biased relative to observations (23).

164 Wind-induced variability, including the seasonal cycle in surface wind stress, also contributes
165 noticeably to anomalies in the overturning across OSNAP-EAST ($R=0.68$, Figure 2c). However, winds do not
166 overwhelmingly dominate the subpolar AMOC as they do at 26°N . If we consider only wind stress anomalies
167 relative to the seasonal cycle, they explain 31% of the variability at OSNAP-EAST ($R=0.56$). Anomalies in
168 SST and SSS relative to the seasonal cycle jointly explain a smaller but comparable fraction, 12% of variability
169 ($R=0.35$) in the OSNAP-EAST AMOC as represented in ECCO. SST and SSS anomalies drive inter-annual

170 variability in the OSNAP-EAST circulation that is similar in magnitude to the large background seasonal cycle
 171 in overturning (Figure 3a). All of these components – due to wind stress, SST, and SSS – combine to generate
 172 variability at the OSNAP-EAST array that can be largely explained by a geostrophic balance between the
 173 Coriolis force and pressure gradients even on inter-monthly timescales (Extended Data Figure ED3). We note
 174 that this is in contrast to variability at the RAPID-MOCHA line, where geostrophic balance dominates only at
 175 low frequencies (Extended Data Figure ED3, 4, 24, 25).

176



177 **Figure 3. Contributions of sea-surface salinity and temperature to variability in**
 178 **overturning.** Sea surface salinity (gray) and temperature (brown) contributions to the
 179 total buoyancy component (yellow) of the OSNAP-EAST (a) and RAPID-AMOC (b)
 180 reconstructions. The estimates use sets of sensitivity patterns based on a linearization
 181 of the model over a single historical period (See Methods), while the full reconstructions in
 182 Figure 2 use linearization over two historical periods to estimate uncertainty. For
 183 comparison, vertical black bars indicate the amplitude of the seasonal cycle in RAPID

184 and OSNAP-EAST overturning in ECCO. The timeseries of contributions to RAPID-
 185 MOCHA overturning begin in 1998 because a 6-year memory of SST and SSS is
 186 required (See Methods), and the observationally constrained state estimate begins in
 187 1992.

188 At both subtropical and subpolar latitudes, SSS-induced AMOC variability is significantly
 189 anti-correlated with SST-induced AMOC variability (Figure 3). To explore this relationship, we
 190 consider the AMOC sensitivity to surface boundary conditions in particular periods of the ECCO state
 191 estimate (See Methods). The estimated SST and SSS contributions to OSNAP-EAST variability
 192 shown in Figure 3a are anticorrelated with $R=-0.42$. This statistical relationship indicates a partial
 193 compensation between the SSS- and SST-driven contributions to historical AMOC changes.
 194 Generally, the variability due to SSS dominates over that due to SST at OSNAP-EAST (Figure 3a),
 195 while at 26°N this is not the case (Figure 3b).

196

197 *Spatial origins of AMOC variability*

198 Figure 4 shows the spatial origins of the AMOC variability that results from anomalies in zonal wind
 199 stress (a,e), meridional wind stress (b,f), SST (c,g) and SSS (d,h). Plotted is the root-mean-square
 200 contribution per unit area [Sv m^{-2}] to the convolutions in equation (1) over the period 1992-2015:

$$201 \quad C_{\mathcal{P}}(\mathbf{x}) = \frac{1}{A(\mathbf{x})} \sqrt{\frac{1}{(T_f \cdot \tau)} \sum_{t=0}^{T_f} \sum_{t'=\max(t-\tau,0)}^t [\mathcal{P}(\mathbf{x}, t') \mathcal{G}_{\mathcal{P}}(t; \mathbf{x}, t - t')]^2} \quad (2)$$

202 where $A(\mathbf{x})$ is the horizontal surface area of the model grid cell in location \mathbf{x} , \mathcal{P} represents the surface field

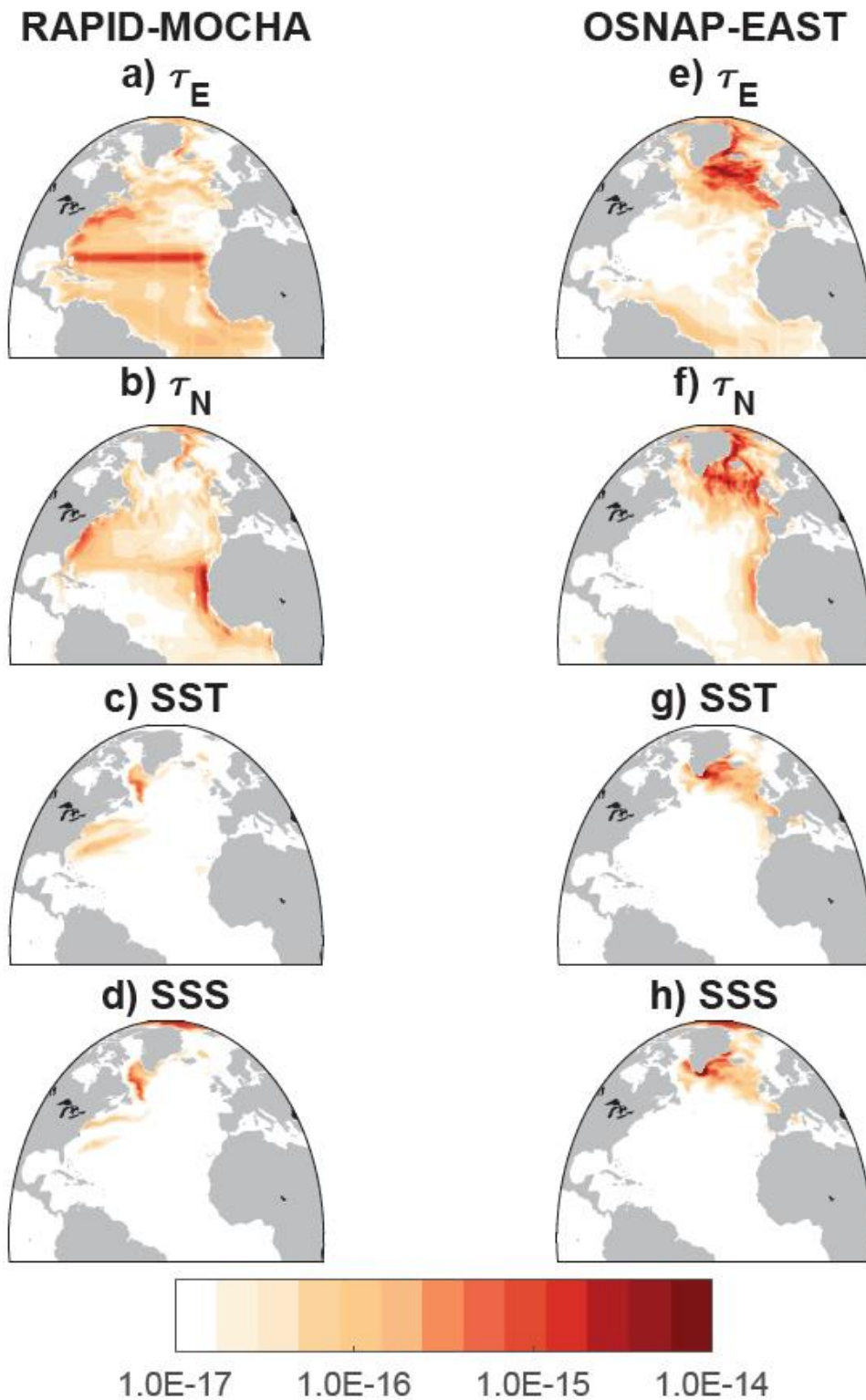
203 anomalies relative to the climatology at a lead time t' summed up to a finite maximum memory τ . The

204 function $\mathcal{G}_{\mathcal{P}}$ is the corresponding sensitivity pattern that depends on the season, the lead time t' , and the

205 geographical location \mathbf{x} as in equation (1). We sum the convolution of \mathcal{P} and $\mathcal{G}_{\mathcal{P}}$ until the end of the

206 available timeseries $t = T_f$ and compute the root-mean-square (See Methods). In effect, the convolution

207 in equation (2) allows us to identify the regions where variability in wind stress, SST, and SSS most
208 strongly projects onto the corresponding AMOC sensitivity patterns and activates them (Figure 4).



209

210 **Figure 4. Spatial origins of variability in overturning at the RAPID-MOCHA (a-d)**
211 **and OSNAP-EAST (e-h) arrays. Color indicates the root-mean-square contribution**

212 per unit area [Sv m^{-2}] to the convolutions in equation (1) over the period 1992-2015
213 using sensitivity patterns based on a linearization of the model over a historical period
214 (See Methods). Contributions due to zonal (a,e) and meridional (b,f) windstress, SST
215 (c,g), and SSS (d,h) all relative to the seasonal cycle. The scale is logarithmic.

216 Local winds dominate AMOC variability at 26°N (11) via two mechanisms: 1) Winds
217 generate meridional transport anomalies within the Ekman surface boundary layer (22); and 2)
218 wind stress induces Rossby wave undulations of the thermocline that propagate westward and
219 cause density anomalies along the western boundary of the Atlantic (24). This build-up of
220 density anomalies alters the balance between east-west pressure gradients in the ocean and the
221 Coriolis force, thus changing the meridional transport (22) across the RAPID-MOCHA array.
222 Remote winds play a larger role in generating variability in the overturning across OSNAP-
223 EAST. For example, wind-driven coastal waves propagating along the boundaries transmit the
224 impact of variability in subtropical and subarctic wind stress to the Subpolar North Atlantic
225 (Figure 4f). These waves give rise to density anomalies on the Scottish and Greenland shelves
226 and hence affect the balance between ocean pressure gradients along the OSNAP-EAST array
227 and the Coriolis force. As a result, transport across the array changes. A similar waveguide
228 mechanism along the Atlantic's eastern boundary has also been identified in studies exploring
229 the sensitivity of Labrador Sea heat content (26), heat transport across the Iceland-Scotland
230 Ridge (27), and bottom pressure in the Arctic (28) to surface boundary conditions.

231 The overturning at OSNAP-EAST is also strongly influenced by local SSS and SST
232 anomalies along the eastern coast of Greenland (Figure 4 g,h). This reflects two factors: (a) the
233 existence of large thermohaline variability in the region, and (b) the impact of density
234 anomalies at the boundary on the balance between ocean pressure gradients and the Coriolis
235 force. Note, however, that SST and SSS anomalies at these locations may be set by air-sea

236 fluxes of heat and freshwater over a much larger geographical area and over a period of several
237 years (See Extended Data Figure ED4).

238 The buoyancy-forced component of the AMOC at 26°N exhibits long-term variability that
239 arises from non-local surface buoyancy anomalies, namely those in the Arctic and the Labrador Sea
240 (Figure 4c,d). Previous studies have suggested that deep convection in the Labrador Sea is related to
241 subtropical AMOC variability on interannual and longer time scales (29, 30). We note that in the
242 ECCO state estimate, there is deep convection both near the western boundary and in the interior of
243 the Labrador Sea. However, the largest contribution of subpolar SST and SSS anomalies to
244 reconstructed variability in RAPID-MOCHA overturning is concentrated in a narrow region near the
245 western boundary of the subpolar basin (Figure 4c,d and Extended Data Figure ED5). This region is
246 known to play a key role in the ventilation of deep water masses in the Labrador Sea (31). In contrast,
247 surface buoyancy anomalies in the convective interior of the Labrador Sea make a smaller contribution
248 to variability at RAPID-MOCHA. This result demonstrates that the causal connection between water
249 mass transformation in the Labrador Sea and the subtropical AMOC is complex. As previously
250 suggested (19), the background ocean circulation can advect density anomalies from the Labrador Sea
251 towards the eastern subpolar gyre where they imprint (32) on Lower North Atlantic Deep Water
252 (LNADW), the densest water mass in the AMOC lower limb. Anomalies in the volume and density
253 of the LNADW layer can then be communicated to the subtropics at depth along the North Atlantic
254 western boundary, and via ocean interior pathways, reaching 26°N on a timescale of approximately 4
255 years (33).

256

257 *Implications for understanding future AMOC changes*

258 Our analysis has shown that a large fraction of the observed and simulated variability
259 in the Atlantic overturning circulation across the OSNAP-EAST array in the subpolar gyre,

260 and across the RAPID-MOCHA array at 26°N, can be reconstructed using best estimates of
261 historical SST, SSS, and wind anomalies, convolved with AMOC sensitivity patterns
262 computed from the adjoint of an ocean circulation model. This allows us to unambiguously
263 attribute recent historical changes to particular sources of variability. At 26°N, the impact of
264 remote (subpolar) surface buoyancy anomalies emerges only on decadal timescales (Figure
265 3b). On shorter timescales, almost all of the variability in overturning can be reconstructed
266 from knowledge of the past wind forcing alone (11, and see Figure 2d). However, our analysis
267 suggests that reconstructing and predicting the overturning at the latitude of the OSNAP-EAST
268 array presents a greater challenge because wind stress and surface buoyancy anomalies each
269 explain a comparable fraction of the total variability in the subpolar circulation on inter-annual
270 to decadal timescales. This provides strong motivation for continued observation of the AMOC
271 by the OSNAP array in order to monitor and understand the state of the overturning circulation
272 in that region and ultimately detect any anthropogenic influence.

273 Our results also confirm that sustained observation of SST and SSS anomalies in the
274 subpolar North Atlantic, e.g. along the OSNAP-WEST line (see Figure 1 and Figure 4 c, d),
275 may give us predictability for the buoyancy-induced decadal trend in the subtropical AMOC
276 at the RAPID-MOCHA array. However, our reconstruction suggests that, compared to the
277 subtropics, the overturning circulation in the subpolar North Atlantic is more sensitive to
278 changes in the background ocean state (Figure 2, compare the size of the shaded gray envelope
279 of uncertainty in a and b) such as shifts in the sites of deep convection. This implies that future
280 climate change may alter the inter-annual variability in the OSNAP-EAST overturning as well
281 as its response to local and remote surface buoyancy anomalies. Attributing, understanding,
282 and predicting changes in AMOC transport at both subpolar and subtropical latitudes therefore

283 hinges on the continued observation of the overturning (3,4,5) and of the background ocean
284 state (34) as part of a coordinated Atlantic observation system.

285

286 **References**

- 287 1. Lozier, M.S., 2012. Overturning in the North Atlantic. *Annual Review of Marine*
288 *Science*, **4**, 291-315.
- 289 2. Stolpe, M., Medhaug, J. Sedláček , and R. Knutti (2018). Multidecadal Variability in
290 Global Surface Temperatures Related to the Atlantic Meridional Overturning
291 Circulation. *Journal of Climate*. **31**. 10.1175/JCLI-D-17-0444.1.
- 292 3. S.A. Cunningham, T. Kanzow, D. Rayner, M.O. Baringer, W.E. Johns, J. Marotzke, H.
293 R. Longworth, E. M. Grant, J. J.-M. Hirschi, L. M. Beal, C. S. Meinen, H.
294 L. Bryden, Temporal variability of the Atlantic meridional overturning circulation at
295 26.5°N. *Science* **317**, 935 – 938 (2007).doi:10.1126/science.1141304pmid:17702940
- 296 4. Smeed, D. A., Josey, S. A., Beaulieu, C., Johns, W. E., Moat, B. I., Frajka-Williams, E.,
297 et al. (2018). The North Atlantic Ocean is in a state of reduced overturning. *Geophysical*
298 *Research Letters*, **45**, 1527– 1533. <https://doi.org/10.1002/2017GL076350>
- 299 5. Lozier, M.S., S. Bacon, A. S. Bower, S. A. Cunningham, M. Femke de Jong, L. de
300 Steur, B. deYoung, J. Fischer, S. F. Gary, B. J. W. Greenan, P. Heimbach, N.P. Holliday,
301 L. Houpert, M.E. Inall, W.E.Johns, H.L. Johnson, J. Karstensen, F. Li, X. Lin, N.
302 Mackay, D.P. Marshall, H. Mercier, P.G.Myeres, R.S. Pickart, H.R. Pillar, F. Straneo, V.
303 Thierry, R.A. Weller, R.G. Williams, C. Wilson, J. Yang, J. Zhao, J. D. Zika,Overturning
304 in the Subpolar North Atlantic Program: A new international ocean observing system.
305 *Bull. Am. Meteorol. Soc.* **98**, 737 – 752 (2017). doi:10.1175/BAMS-D-16-0057.1

- 306 6. Biastoch, A., C. W. Böning, J. Getzlaff, J.-M. Molines, and G. Madec, 2008: Causes of
307 interannual–decadal variability in the meridional overturning circulation of the North
308 Atlantic Ocean. *J. Climate*, 21, 6599–6615, doi:10.1175/2008JCLI2404.1.
- 309 7. Polo, I., J. Robson, R. Sutton, and M. A. Balmaseda, 2014: The importance of wind and
310 buoyancy forcing for the boundary density variations and the geostrophic component of
311 the AMOC at 26°N. *J. Phys. Oceanogr.*, **44**, 2387–2408, [https://doi.org/10.1175/JPO-D-](https://doi.org/10.1175/JPO-D-13-0264.1)
312 13-0264.1
- 313 8. Ortega, P., Robson, J., Sutton, R.T. et al. (2017) Mechanisms of decadal variability in the
314 Labrador Sea and the wider North Atlantic in a high-resolution climate model. . *Clim*
315 *Dyn.*, **49**: 2625-2647. <https://doi.org/10.1007/s00382-016-3467-y>
- 316 9. R.M. Errico. (1997) What is an adjoint model?, *Bull. Am. Meteorol. Soc.*, **78**, 2577-
317 2591, 10.1175/1520-0477(1997) 078<2577:WIAAM>2.0.CO;2
- 318 10. Forget, G., J.M. Campin, P. Heimbach, C.N. Hill, R.M. Ponte, and C. Wunsch, 2015:
319 ECCO version 4: an integrated framework for non-linear inverse modeling and global
320 ocean state estimation. *Geosci. Model Dev.*, **8**, 3071-3104.
- 321 11. Pillar, H., P. Heimbach, H. Johnson, and D. Marshall, 2016: Dynamical attribution of
322 recent variability in Atlantic overturning. *J. Climate*, 29, 3339-3352,
323 doi:<https://doi.org/10.1175/JCLI-D-15-0727.1>.
- 324 12. Smith, T. and P. Heimbach. 2019. Atmospheric origins of variability in the South
325 Atlantic meridional overturning circulation. *J. Clim.*, **32(5)**, 1483-1500,
326 doi:10.1175/JCLI-D-18-0311.1.
- 327 13. Giering, R., 2010: Transformation of algorithms in Fortran Version 1.15 (TAF Version
328 1.9.70). FastOpt.

- 329 14. Fukumori, I., O. Wang, I. Fenty, G. Forget, P. Heimbach, and R. M. Ponte, 2017: ECCO Version 4
330 Release 3, *NASA-JPL*. <http://hdl.handle.net/1721.1/110380>, doi:1721.1/110380.
- 331 15. Marshall, J., C. Hill, L. Perelman, and A. Adcroft, Hydrostatic, quasi-hydrostatic, and
332 nonhydrostatic ocean modeling, *J. Geophys. Res.*, **102(C3)**, 5733-5752, 1997b
- 333 16. Forget, G., Ferreira, D., and Liang, X.: On the observability of turbulent transport rates
334 by Argo: supporting evidence from an inversion experiment, *Ocean Sci.*, **11**, 839–853,
335 <https://doi.org/10.5194/os-11-839-2015>, 2015
- 336 17. Fukumori, I., Heimbach, P., Ponte, R. M., and Wunsch, C. (2018). A dynamically
337 consistent, multivariable ocean climatology. *Bull. Am. Meteorol. Soc.* **99**, 2107–2128.
338 doi: 10.1175/BAMS-D-17-0213.1
- 339 18. Jackson, L. C., Dubois, C., Forget, G., Haines, K., Harrison, M., Iovino, D., et al. (2019).
340 The mean state and variability of the North Atlantic circulation: A perspective from
341 ocean reanalyses. *Journal of Geophysical Research: Oceans*, **124**, 9141–9170.
342 <https://doi.org/10.1029/2019JC015210>
- 343 19. Lozier, M.S., Li, F., Bacon, S., Bahr, F., Bower, A. S., Cunningham, S. A., et al. (2019).
344 A sea change in our view of overturning in the subpolar North Atlantic. *Science* **363**,
345 516–521. doi: 10.1126/science.aau6592
- 346 20. Li, F., M.S. Lozier and W. Johns, 2017. Calculating the meridional volume, heat and
347 freshwater transports from an observing system in the subpolar North Atlantic:
348 Observing system simulation experiment. *Journal of Atmospheric and Oceanic*
349 *Technology*, doi: 10.1175/JTECH-D-16-0247.1
- 350 21. Desbruyères, D.G, H. Mercier, G. Maze, N. Danialt (2019). Surface predictor of
351 overturning circulation and heat content change in the subpolar North Atlantic. *Ocean*
352 *Science* , **15(3)**, 809-817. <https://doi.org/10.5194/os-15-809-2019>

- 353 22. Marshall, J., and A. Plumb (2008), *Atmosphere, Ocean, and Climate Dynamics: An*
354 *Introductory Text*, Elsevier, Amsterdam.
- 355 23. Menary, M. B., Hermanson, L., & Dunstone, N. J. (2016). The impact of Labrador Sea
356 temperature and salinity variability on density and the subpolar AMOC in a decadal
357 prediction system. *Geophysical Research Letters*, 43, 12,217–12,227.
358 <https://doi.org/10.1002/2016GL070906>
- 359 24. Zhao, J., & Johns, W. (2014b). Wind-forced interannual variability of the Atlantic
360 meridional overturning circulation at 26.5°N. *Journal of Geophysical Research:*
361 *Oceans*, **119(4)**, 2403–2419. <https://doi.org/10.1002/2013JC009407>
- 362 25. Kanzow, T. et al., 2010: Seasonal Variability of the Atlantic Meridional Overturning
363 Circulation at 26.5°N. *J. Climate*, **23**, 5678–5698,
364 <https://doi.org/10.1175/2010JCLI3389.1>.
- 365 26. Jones, D. C., Forget, G., Sinha, B., Josey, S. A., Boland, E. J. D., Meijers, A. J. S., et al.
366 (2018). Local and remote influences on the heat content of the Labrador sea: an adjoint
367 sensitivity study. *J. Geophys. Res. Oceans* **123**, 2646–2667. doi: 10.1002/2018JC013774
- 368 27. Loose, N., Heimbach, P., Pillar, H. R., & Nisancioglu, K. H. (2020). Quantifying
369 dynamical proxy potential through shared adjustment physics in the North
370 Atlantic. *Journal of Geophysical Research: Oceans*, 125,
371 e2020JC016112. <https://doi.org/10.1029/2020JC016112>
- 372 28. Fukumori, I., Wang, O., Llovel, W., Fenty, I., and Forget, G. (2015). A near-uniform
373 fluctuation of ocean bottom pressure and sea level across the deep ocean basins of the
374 Arctic Ocean and the Nordic Seas. *Progr. Oceanogr.* **134**, 152–172. doi:
375 10.1016/j.pocean.2015.01.013

- 376 29. Eden, C., J. Willebrand, Mechanism of interannual to decadal variability of the North
377 Atlantic circulation. *J. Clim.* 14, 2266–2280 (2001). doi:10.1175/1520-
378 0442(2001)014<2266:MOITDV>2.0.CO;2
- 379 30. Getzlaff, J., C. W. Böning, C. Eden, A. Biastoch, Signal propagation related to the North
380 Atlantic overturning. *Geophys. Res. Lett.* 32, L09602 (2005).
381 doi:10.1029/2004GL021002
- 382 31. MacGilchrist, G. A., H. L. Johnson, D. P. Marshall, C. Lique, M. Thomas, L. C. Jackson,
383 and R. A. Wood, Locations and mechanisms of ocean ventilation in the high-latitude
384 North Atlantic in an eddy-permitting ocean model. *J. Climate*,
385 doi: <https://doi.org/10.1175/JCLI-D-20-0191.1>.
- 386 32. Zantopp, R., Fischer, J., Visbeck, M., and Karstensen, J. (2017), From interannual to
387 decadal: 17 years of boundary current transports at the exit of the Labrador Sea, *J.*
388 *Geophys. Res. Oceans*, **122**, 1724– 1748, doi:10.1002/2016JC012271.
- 389 33. Zou S, Lozier M.S., Buckley M. (2019) How is meridional coherence maintained in the
390 lower limb of the Atlantic Meridional Overturning Circulation? *Geophys Res Lett* **46**:244–
391 252. <https://doi.org/10.1029/2018GL080958>
- 392 34. Roemmich D., et al. (2019) On the Future of Argo: A Global, Full-Depth, Multi-
393 Disciplinary Array. *Frontiers in Marine Science*, **6**, p. 439,
394 DOI:10.3389/fmars.2019.00439
- 395 35. G.D. McCarthy, et al. (2015) Measuring the Atlantic Meridional Overturning Circulation
396 at 26°N, *Progress in Oceanography*, **130**, 91-111,
397 <https://doi.org/10.1016/j.pocean.2014.10.006>.

398

399

400 *Acknowledgements*

401 This study used the ARCHER UK National Supercomputing Service
402 (<http://www.archer.ac.uk>). In our analysis, we apply the TAF software provided by FastOpt.
403 The maps used in the figures and supplementary material were produced using the freely
404 available software "M_Map: A mapping package for MATLAB", provided by R. Pawlowicz.
405 We thank the groups that maintain the OSNAP and RAPID-MOCHA observational networks
406 and the developers of the ECCO version 4 state estimate. Y.K. was funded by the OSNAP
407 project through NERC grant, NE/K010948/1 and the TICTOC project through NERC grant
408 NE/P019064/1. H.L.J., and D.P.M. were also funded by NERC grant, NE/K010948/1. G.F.
409 acknowledges support from NASA award #6937342 and the Simons Foundation award
410 #549931. P.H., H.R.P., and T.S. were supported in part by NOAA grant
411 NOAA/NA130AR4310135, NSF grant NSF-OCE-1924546, and a JPL/Caltech subcontract.
412 T.S. received additional funding from an Oden Institute CSEM fellowship. N.P.H. was
413 funded by the OSNAP NERC grant NE/K010875/1. M.S.L and F.L. were supported by NSF
414 grants OCE-1948335 and OCE-1924456. The authors thank the editor and the anonymous
415 reviewers.

416
417

418 **Ethics declarations**

419 Competing interests

420 The authors declare no competing interests.

421

422 **Code availability.**

423 The code for the MITgcm and the scripts for post-processing model output are available at
424 <https://github.com/MITgcm/>. The ECCO state estimate model configuration can be
425 downloaded from <https://github.com/gaelforget/ECCOv4>, with initial and boundary
426 conditions available at <https://web.corral.tacc.utexas.edu/OceanProjects/ECCO/ECCOv4>.

427 The TAF algorithmic differentiation software is proprietary and provided by FastOpt. Code
428 used to process data and produce figures is available from the corresponding author Y.K.
429 upon reasonable request.

430

431 **Data availability**

432 The OSNAP data products are publicly available at www.o-snap.org. The derived data
433 including the OSNAP-EAST overturning are furthermore available in Duke Digital
434 Repository, <https://research.repository.duke.edu/collections/1z40kt318>. The RAPID-MOCHA
435 overturning timeseries is available at https://www.rapid.ac.uk/rapidmoc/rapid_data/datadl.php

436

437 **Contributions**

438 All authors discussed the results and contributed to the preparation of the final manuscript. Y.K. took
439 the lead in writing the text while holding regular discussions with H.L.J., D.P.M., T.S., and H.R.P.
440 Y.K. planned, designed, and performed the adjoint sensitivity analysis with the MITgcm. P.H. and
441 G.F. developed and maintained the ECCO version 4 state estimate and the associated tools for post-
442 processing MITgcm output on an irregular grid. T.S. adapted the MITgcm diagnostic package.
443 N.P.H., F.L., and M.S.L. developed and applied the data analysis methodology for OSNAP
444 observations, and F.L. provided the OSNAP-EAST overturning time series.

445 METHODS

446 We use an algorithmic differentiation software, Transformation of Algorithms in FORTRAN
447 (TAF, 1), to obtain the adjoint of the MIT ocean general circulation model (MITgcm) in the ECCO
448 (Estimating the Circulation and Climate of the Ocean) version 4 (v4) configuration (2), whose
449 release 3 covers the 1992-2015 period. The ECCOv4 state estimate reproduces very skillfully the
450 observed subtropical AMOC at the RAPID-MOCHA array (Rapid Climate Change – Meridional
451 Overturning Circulation and Heatflux Array). If we detrend and smooth the intermonthly timeseries
452 with a twelve-month running mean, the correlation between the state estimate and the RAPID-
453 MOCHA observations is $R=0.83$ (significant at the 1% level). In terms of the low-frequency
454 variability, the RAPID-MOCHA overturning represented in ECCOv4 does not show the same 2004-
455 2006 positive anomaly as in the direct observational estimate. Hence, ECCOv4 underestimates the
456 subsequent decline at RAPID-MOCHA after 2006. Furthermore, towards the end of the
457 observational record, there is a mismatch in the high frequency variability between ECCOv4 and
458 RAPID-MOCHA observations despite the good agreement overall. The OSNAP (Overturning in
459 the Subpolar North Atlantic Program) observational record is too short to compute correlations with
460 the ECCO historical state estimate. However, the ECCO timeseries mostly agree with the direct
461 observational estimate at OSNAP-EAST within the observational uncertainty.

462 In this study, we modify the adjoint code of the MITgcm ECCO configuration and set up
463 numerical calculations that output sensitivity patterns for the response of the Atlantic overturning to
464 SST and SSS, as well as the response to surface wind stress assuming constant SST and SSS, at
465 different lead times. Our objective functions for each adjoint calculation are defined in terms of
466 volume transport in Sverdrups ($1 \text{ Sv} = 10^6 \text{ m}^3\text{s}^{-1}$).

467 We compute seasonal sensitivity patterns of the February, May, August, and November
468 monthly-averaged overturning and for computational efficiency assume these to be representative

469 of the winter, spring, summer, and fall objective functions, respectively. This simplification
470 introduces an annually cyclic bias in the buoyancy-related components of our reconstruction (see the
471 apparent small oscillation in Figure 3 of the main text). Nevertheless, it is clear to see that the
472 oscillations that arise due to this computational choice are small and with nearly compensating
473 effects in the SST and SSS components. Hence, this does not affect our conclusions.

474 We perform two sets of adjoint calculations each yielding the seasonally-dependent linear sensitivity
475 of the overturning at two different regions in the North Atlantic. First, we perform a set of calculations that
476 give us the lagged sensitivity of the AMOC volume transport at 26°N in depth space to surface anomalies at
477 different lead times and horizontal locations. Calculations for the AMOC strength at 26°N in potential density
478 space give similar sensitivity results. Second, we perform an analogous set of calculations for the lagged
479 sensitivity of the density-space overturning across the OSNAP-EAST line. To be consistent with observational
480 products from the OSNAP array, we use potential density coordinates, referenced to the surface. The Eulerian
481 velocity components at the vertical walls of each model grid cell are binned into different layers depending on
482 the potential density interpolated onto the cell boundaries. We then obtain the OSNAP-EAST overturning by
483 integrating the velocity across the array vertically, going from denser to lighter layers.

484 The sensitivity patterns we obtain depend on the time-evolving ocean state about which we
485 linearize the model. To assess this non-linear effect, we compute each set of sensitivity patterns
486 twice, linearizing about two different periods of the ECCO state estimate: one ending in 2001-2002
487 and one in 2006-2007. We select these two representative periods, ending 10 and 15 years into the
488 ECCO run, because the earlier years of the state estimate are marked by unusually strong convection
489 in the subpolar North Atlantic. Computational cost limits our ability to repeat the adjoint calculation
490 over additional time periods. We consider both the mean and the spread between the two estimates
491 and use each of them to reconstruct the AMOC timeseries and to identify sources of variability in
492 Atlantic overturning. Figures 3 and 4 in the Main Text show sources of variability in the AMOC

493 based on a linearization of the model over the historical period ending in 2006-2007. In comparison,
 494 Figure S2 in the SI presents an analogous estimate but using a linearization over the earlier time period
 495 ending in 2001-2002. When computing correlations, we use the mean of the two reconstructions.

496 In our reconstructions we consider sensitivity to SST and SSS, rather than fluxes of heat
 497 and freshwater across the air-sea interface, because the former are more readily constrained by
 498 available in-situ and satellite observations of the ocean. Moreover, air-sea fluxes are a step
 499 further removed from surface buoyancy compared to temperature and salinity. The ocean
 500 integrates local and remote surface fluxes, which then gives rise to SST and SSS anomalies.
 501 Therefore, if we used AMOC sensitivity to surface fluxes, we would have to consider much
 502 longer lead times, at which the adjoint of the MITgcm becomes less reliable (see a discussion
 503 in 3,5). For example, we would need accurate sensitivity to surface fluxes all along the Gulf
 504 Stream and the North Atlantic Current advective pathways going back years (See Extended
 505 Data Figure ED4).

506 We convolve the sensitivity patterns from each set of adjoint calculations with 1992 – 2015 historical
 507 estimates of wind stress, SST, and SSS anomalies from the ECCO ocean state estimate. We define anomalies
 508 in these fields relative to the climatological seasonal cycle. However, when exploring the wind contribution
 509 to AMOC variability (Fig. 2c,d), we also separately consider the impact of the climatological seasonal cycle
 510 in surface wind stress. Each convolution gives us an estimate for the time-evolving contribution $C_{\mathcal{P}}$ of a given
 511 ocean surface field \mathcal{P} to historical variability in the rate of overturning:

$$512 \quad C_{\mathcal{P}}(t) = \int_{t-\tau}^t \int \mathcal{P}(\mathbf{x}, t') \mathcal{G}_{\mathcal{P}}(t; \mathbf{x}, t - t') d\mathbf{x} dt' \quad (\text{S1})$$

513 where \mathcal{P} is the surface field anomaly relative to the climatological monthly mean. The function $\mathcal{G}_{\mathcal{P}}$
 514 denotes the sensitivity pattern that depends on the season at time t , the lead time t' , and the geographical
 515 location \mathbf{x} . In order to remove numerical noise, the patterns of sensitivity to SST and SSS are smoothed using
 516 a diffusive Gaussian operator (3,4) with a spatial decorrelation scale of two grid cells. This operator is not

517 applied to wind stress sensitivity patterns, vector fields on an irregular model grid. The integration in space
518 \mathbf{x} is over the whole global ocean surface, and the time integration goes back to a cutoff lead time τ
519 representing the assumed maximum memory of the AMOC to past forcing. The cutoff lead times are
520 as follows: 3 years for wind stress in OSNAP-EAST reconstructions, 2 years for SST and SSS in
521 OSNAP-EAST reconstructions, and 6 years for all components in RAPID AMOC reconstructions. In
522 reality, the ocean circulation retains memory of previous forcing on much longer timescales. However,
523 nonlinear effects are larger at longer lead times and the adjoint of the MITgcm cannot capture them
524 (see a discussion in 3, 5). By sweeping parameter space in t' , we have established that when we increase
525 the cutoff lead times beyond the appropriate ranges we identify, our reconstruction skill decreases.
526 This is likely due to the growth of nonlinear error terms at longer lead times. On the other hand, cutoff
527 lead times that are unnecessarily short lead to omission of useful information about past forcing.

528 When computing the contributions due to wind stress, we use AMOC sensitivity patterns
529 representative of 5-day steps in lead-time. We convolve these sensitivity patterns with 5-day mean
530 wind stress fields from ECCO. When estimating the contributions due to surface buoyancy, we use
531 10-day means for the SST, the SSS, and the corresponding sensitivity patterns averaged over 10-day
532 lead-time windows. Even though the ECCO configuration is nominally at a $1^\circ \times 1^\circ$ horizontal
533 resolution, we need this sub-monthly temporal resolution because of the high-frequency, spatially
534 localized wintertime convective variability in the subpolar North Atlantic. Summing the contributions
535 due to wind stress, SST, and SSS anomalies provides a partial reconstruction of the historical
536 variability in the Atlantic overturning circulation relative to the seasonal cycle. Finally, we combine
537 our reconstruction with the 1992-2015 climatological seasonal cycle in Atlantic overturning based on
538 the ECCO state estimate. Note that the OSNAP-EAST observational record is too short to estimate
539 the background seasonal climatology in overturning. Furthermore, analysis of the OSNAP-EAST

540 timeseries in ECCO suggests that variability relative to the seasonal cycle is comparable in amplitude
 541 to the seasonal cycle in subpolar overturning.

542 In this study, we identify the regions where variability in wind stress, SST, and SSS
 543 most strongly projects on the corresponding AMOC sensitivity patterns and activates them.
 544 We consider the root-mean-square contribution per unit area [Sv m^{-2}] to the convolutions in
 545 equation (1) over the period 1992-2015:

$$546 \quad C_{\mathcal{P}}(\mathbf{x}) = \frac{1}{A(\mathbf{x})} \sqrt{\frac{1}{(T_f \cdot \tau)} \sum_{t=0}^{T_f} \sum_{t'=\max(t-\tau, 0)}^t [\mathcal{P}(\mathbf{x}, t') \mathcal{G}_{\mathcal{P}}(t; \mathbf{x}, t - t')]^2} \quad (\text{S2})$$

547 where $A(\mathbf{x})$ is the horizontal surface area of the model grid cell in location \mathbf{x} , \mathcal{P} represents the
 548 surface field anomalies relative to the climatology at a lead time t' summed up to a finite
 549 maximum memory τ , as in equation (S1). The function $\mathcal{G}_{\mathcal{P}}$ is the corresponding sensitivity
 550 pattern that depends on the season, as in equation S1 in the Methods. We sum the convolution
 551 of \mathcal{P} and $\mathcal{G}_{\mathcal{P}}$ until the end of the available timeseries $t = T_f$ and compute the root-mean-
 552 square.

553 We acknowledge that the AMOC sensitivity patterns, reconstructions, and attributions
 554 presented here are based on a model that approximates processes in the ocean. For example, the regions
 555 of deep wintertime convection in the North Atlantic are known to differ widely across climate models
 556 (6). Moreover, the ECCO configuration of the MITgcm that we use does not resolve mesoscale ocean
 557 eddies whose important role in the circulation is instead represented via a widely used
 558 parameterization. Nevertheless, since ECCO formally calibrates the spatially varying parameters in
 559 the model's eddy transport scheme using observational constraints (7), the evolving state of the ocean
 560 in ECCO closely tracks historical temperature, salinity, and ocean circulation conditions (8).

561 We compare our model-based results with observational data from the RAPID-MOCHA array
 562 at 26°N and the OSNAP arrays in the subpolar North Atlantic.

563 In the subpolar latitudes, recent and pre-existing OSNAP moorings on the basin boundaries
564 measure temperature, salinity, density, and velocity (9,10). Away from the OSNAP moorings, an
565 objective analysis method is used to interpolate between these measurements using data from Argo
566 profiles (e.g., 11) and OSNAP gliders, as well as World Ocean Atlas 2013 climatology (12). In
567 addition, away from the arrays, Ekman velocities are estimated from ERA-Interim wind fields (13).
568 This wind-driven ageostrophic transport is assumed to be confined to the Ekman surface boundary
569 layer (14). Geostrophic velocity (14) is estimated using two different reference velocities. Wherever
570 deep moorings are available, their velocity measurements are used as a reference, except in the western
571 Labrador Sea and the central Iceland Basin. Otherwise, time-mean surface velocity data from satellite
572 altimetry provides the reference velocity. Finally, to guarantee a zero net mass transport across the
573 entire OSNAP array, a compensation transport term is included at OSNAP-WEST at each time step.
574 The same term is added with the opposite sign across OSNAP-EAST. These compensation terms are
575 distributed uniformly in regions where velocity measurements are not available.

576 We furthermore use publicly available observational data for the subtropical AMOC
577 provided by the RAPID project (15). We bin the RAPID-MOCHA overturning time series into
578 the same 30-day windows as our model output and reconstructions.

579 When comparing timeseries from the state estimate, reconstructions, and observations, we
580 compute correlation coefficients using standard methods for linear regression. When we test the
581 significance of the regression coefficients, we take into account the redness in the spectral properties of
582 the timeseries. Thus, our null hypothesis is not based on a standard normal distribution. Instead, we use
583 an established spectral Monte-Carlo approach for significance testing (16, 17). All regression coefficients
584 cited in this study are significant at the 1% level.

585

586 ***References for the Methods Section***

- 587 1. Giering, R., 2010: Transformation of algorithms in Fortran Version 1.15 (TAF
588 Version 1.9.70). FastOpt.
- 589 2. Fukumori, I., O. Wang, I. Fenty, G. Forget, P. Heimbach, and R. M. Ponte, 2017:
590 ECCO Version 4 Release 3, <http://hdl.handle.net/1721.1/110380>, doi:1721.1/110380.
- 591 3. Kostov, Y., Johnson, H.L. & Marshall, D.P. AMOC sensitivity to surface buoyancy
592 fluxes: the role of air-sea feedback mechanisms. *Clim Dyn* 53, 4521–4537 (2019).
593 <https://doi.org/10.1007/s00382-019-04802-4>
- 594 4. Weaver AT, Courtier P (2001) Correlation modelling on the sphere using a
595 generalized diffusion equation. *QJR Meteorol Soc* 127:1815–1846
- 596 5. Smith, T. and P. Heimbach. 2019. Atmospheric origins of variability in the South
597 Atlantic meridional overturning circulation. *J. Clim.*, **32(5)**, 1483-1500,
598 doi:10.1175/JCLI-D-18-0311.1.
- 599 6. Heuzé, C. North Atlantic deep water formation and AMOC in CMIP5 models. *Ocean*
600 *Sci.* **13**, 609–622 (2017).
- 601 7. Forget, G., J.M. Campin, P. Heimbach, C.N. Hill, R.M. Ponte, and C. Wunsch, 2015:
602 ECCO version 4: an integrated framework for non-linear inverse modeling and global
603 ocean state estimation. *Geosci. Model Dev.*, **8**, 3071-3104.
- 604 8. Forget, G., Ferreira, D., and Liang, X.: On the observability of turbulent transport
605 rates by Argo: supporting evidence from an inversion experiment, *Ocean Sci.*, **11**,
606 839–853, <https://doi.org/10.5194/os-11-839-2015>, 2015.
- 607 9. Lozier, M.S., Bacon, S., Bower, A. S., Cunningham, S. A., Femke de Jong, M., de
608 Steur, L., et al. (2017). Overturning in the Subpolar North Atlantic Program: A new

- 609 international ocean observing system. *Bulletin of the American Meteorological*
610 *Society*, **98**(4), 737–752. <https://doi.org/10.1175/BAMS-D-16-0057.1>
- 611 10. Zantopp, R., Fischer, J., Visbeck, M., and Karstensen, J. (2017), From interannual to
612 decadal: 17 years of boundary current transports at the exit of the Labrador Sea, *J.*
613 *Geophys. Res. Oceans*, **122**, 1724– 1748, doi:10.1002/2016JC012271.
- 614 11. Forget, G., H. Mercier, B. Ferron (2008) Combining Argo profiles with a general
615 circulation model in the North Atlantic. Part 2: Realistic transports and improved
616 hydrography, between spring 2002 and spring 2003. *Ocean Modelling*, **20**, Issue 1,
617 17-34, <https://doi.org/10.1016/j.ocemod.2007.06.002>.
- 618 12. Locarnini, R. A., A. V. Mishonov, J. I. Antonov, T. P. Boyer, H. E. Garcia, O. K.
619 Baranova, M. M. Zweng, and D. R. Johnson (2010), *World Ocean Atlas 2009*,
620 vol. 1, Temperature, Atlas NESDIS **68**, edited by S. Levitus, NOAA, U.S. Gov. Print.
621 Off., Washington, D. C.
- 622 13. Dee, D. P., Uppala, S. M., Simmons, A. J., Berrisford, P., Poli, P., Kobayashi, S, et
623 al. (2011). The ERA-Interim reanalysis: Configuration and performance of the data
624 assimilation system. *Quarterly Journal of the Royal Meteorological*
625 *Society*, **137**, 553–597. <https://doi.org/10.1002/qj.828>
- 626 14. Marshall, J., and A. Plumb (2008), *Atmosphere, Ocean, and Climate Dynamics: An*
627 *Introductory Text*, Elsevier, Amsterdam.
- 628 15. Smeed, D. A., Josey, S. A., Beaulieu, C., Johns, W. E., Moat, B. I., Frajka-Williams,
629 E., et al. (2018). The North Atlantic Ocean is in a state of reduced overturning.
630 *Geophysical Research Letters*, **45**, 1527– 1533.
631 <https://doi.org/10.1002/2017GL076350>

- 632 16. Lund, I. A., 1970: A Monte Carlo method for testing the statistical significance of a
633 regression equation. *J. Appl. Meteor.*, 9, 330–332, [https://doi.org/10.1175/1520-](https://doi.org/10.1175/1520-0450(1970)009<0330:AMCMFT>2.0.CO;2)
634 [0450\(1970\)009<0330:AMCMFT>2.0.CO;2](https://doi.org/10.1175/1520-0450(1970)009<0330:AMCMFT>2.0.CO;2).
- 635 17. Cornish, S. B., Y. Kostov, H. L. Johnson, and C. Lique, 2020: Response of Arctic
636 Freshwater to the Arctic Oscillation in Coupled Climate Models. *J. Climate*, 33, 2533–
637 [2555, https://doi.org/10.1175/JCLI-D-19-0685.1](https://doi.org/10.1175/JCLI-D-19-0685.1).

638

639

640

641

642

643

644

645

646

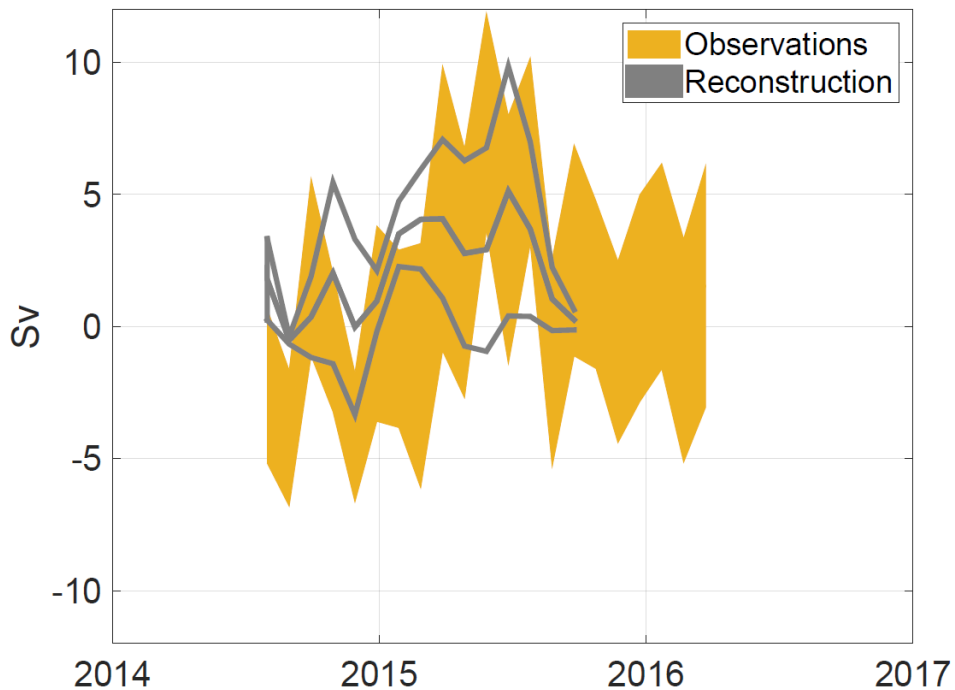
647

648

649

650

651

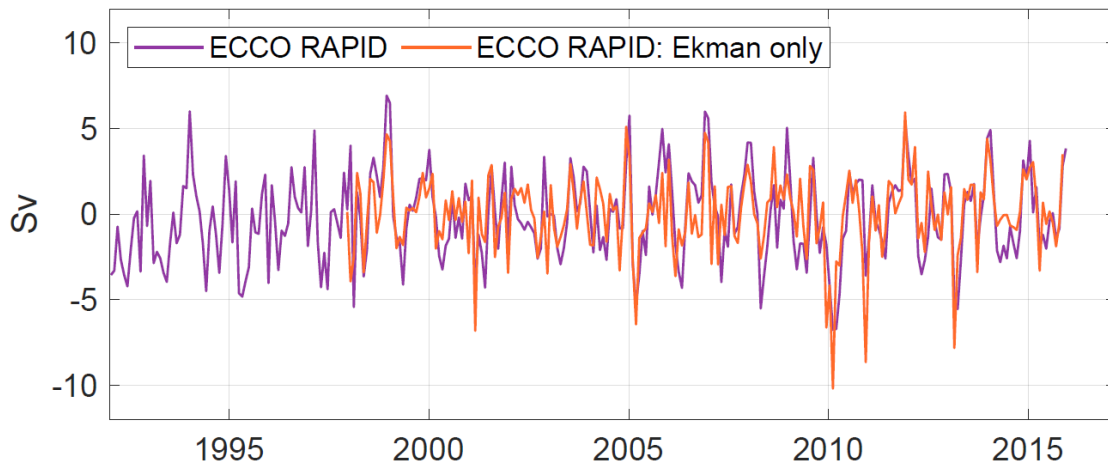


653

654 **Figure ED1. Reconstruction skill for OSNAP-EAST observations.** Comparison
655 between observations (yellow envelope showing ± 1 standard deviation of the
656 observational uncertainty) and our two reconstructions (outer gray contours) of
657 OSNAP-EAST overturning [Sv] based on two different sets of sensitivity patterns: one
658 set from objective functions in 2001-2002, and a second set from objective functions
659 in 2006-2007. The reconstructions are interpolated onto the same 30-day windows as
660 the observations. We consider both the mean of our two reconstructions (middle gray
661 contour) and the spread between them (outer gray contours). Note that our
662 reconstruction estimate uses the ECCOv4r3 mean seasonal cycle, since the
663 observational record at OSNAP-EAST is short.

664

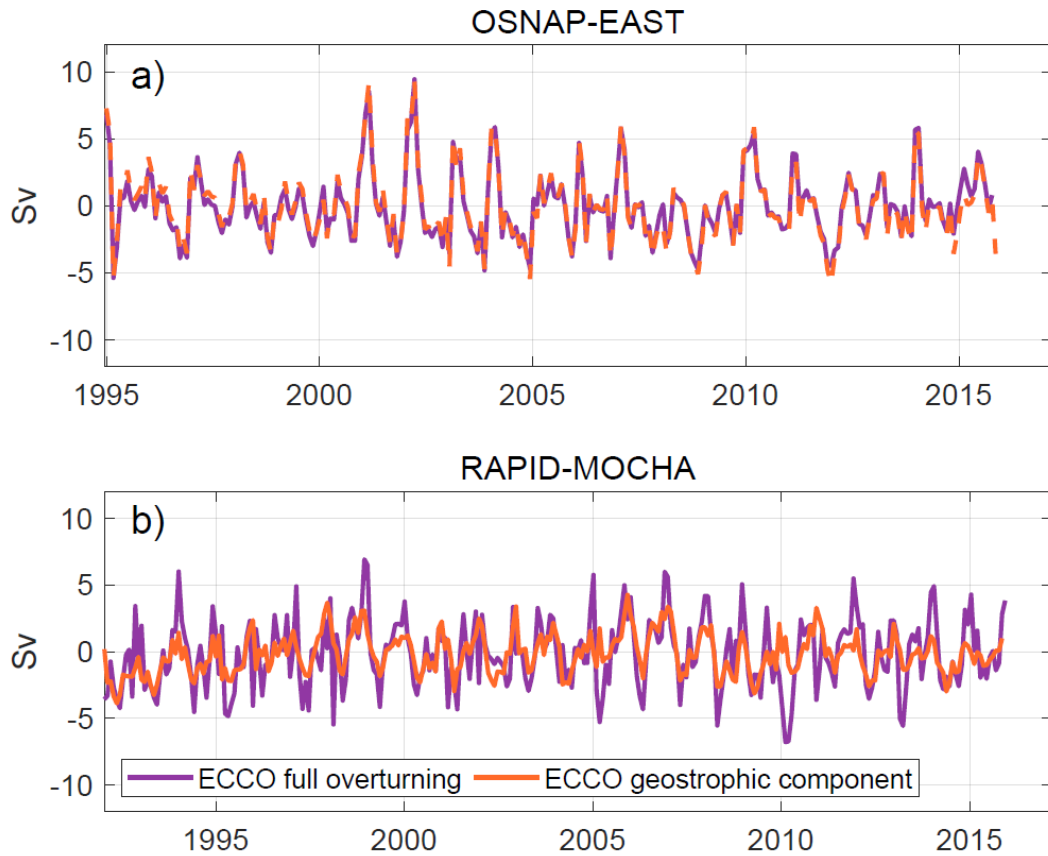
665



666

667 **Figure ED2. Ekman transport contribution to overturning variability at RAPID-**
 668 **MOCHA in ECCO.** ECCO-based comparison between variability in RAPID-MOCHA
 669 overturning (purple) and Ekman transport variability at 26°N (orange) over the time-
 670 period of the linear reconstructions in the main text. Anomalies are shown relative to
 671 the long-term mean.

672



673

674 **Figure ED3. Geostrophic component of overturning in the North Atlantic.**

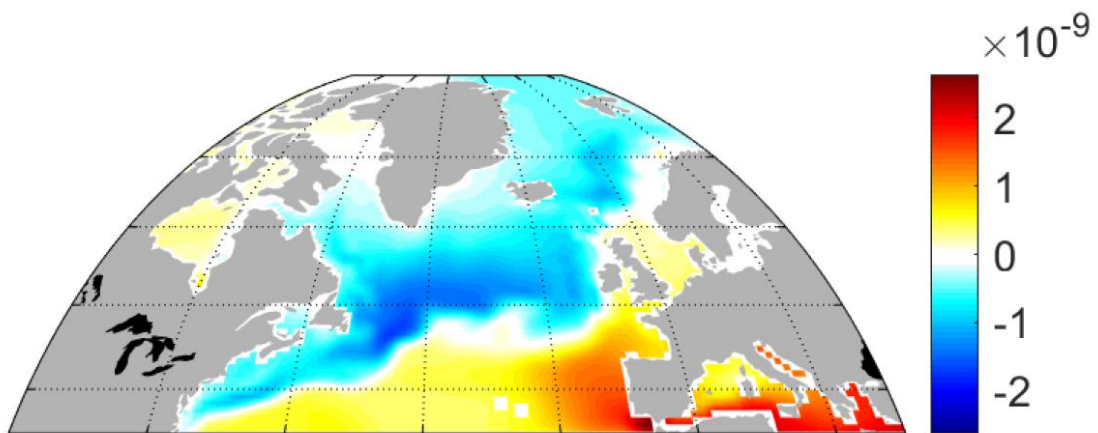
675 Overturning variability (purple, volume transport in Sv) at OSNAP-EAST (a) and
 676 RAPID-MOCHA (b) in the ECCO state estimate contrasted against variability in the
 677 geostrophic component of overturning (orange). The comparison in a spans the time-
 678 period of the linear reconstructions in the main text. Anomalies are shown relative to
 679 the long-term mean.

680

681

682

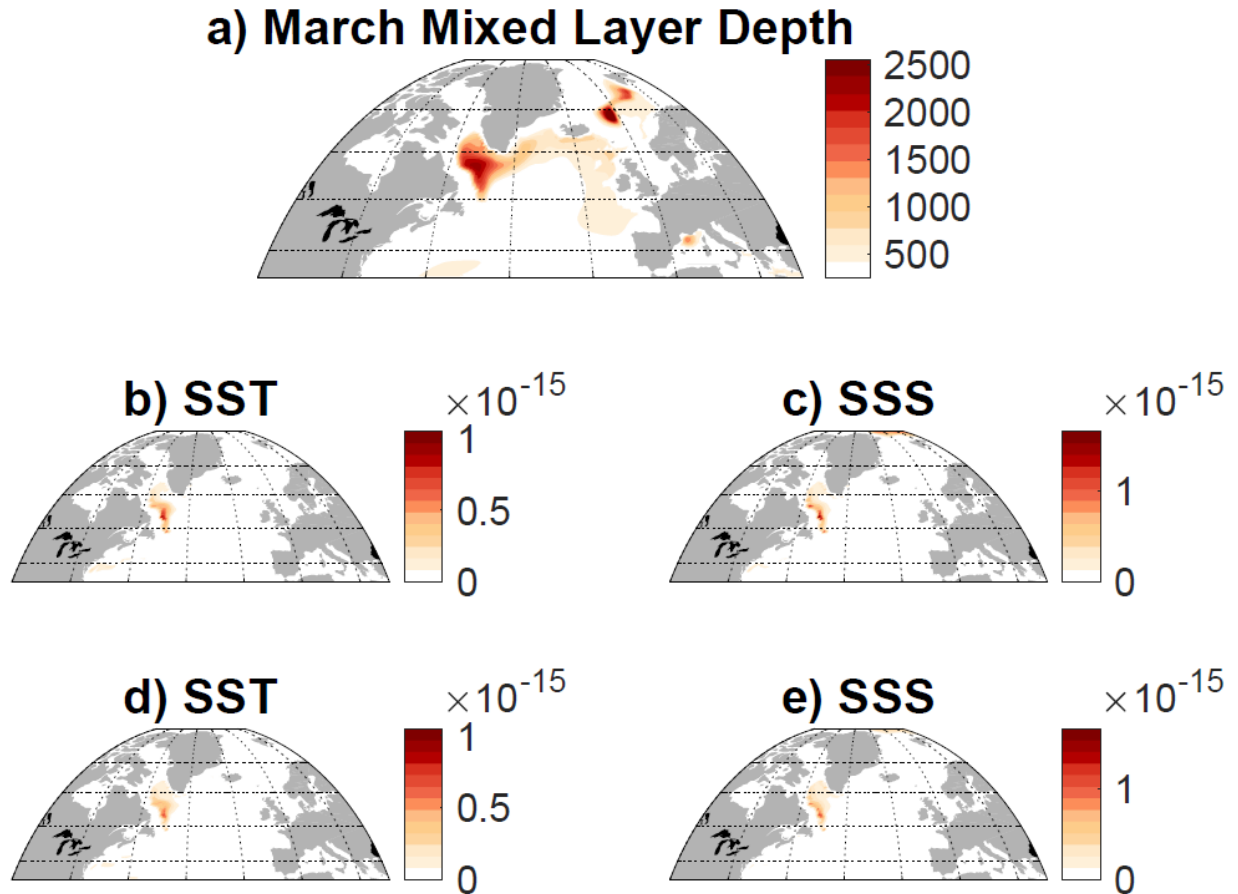
683



684

685 **Figure ED4. Sensitivity of the OSNAP-EAST overturning to surface heat fluxes.**

686 Sensitivity of the OSNAP-EAST overturning in February 2007 to net surface heat fluxes [Sv
 687 per ($W\ m^{-2}$ sustained over 1 hour)] at a lead time of **nine** years. Red shading indicates that
 688 heat flux into the ocean contributes to a delayed strengthening of the OSNAP-EAST
 689 overturning 9 years later. Blue shading indicates that cooling the ocean surface at that lead
 690 time causes a lagged strengthening of the OSNAP-EAST overturning. Notice the pattern
 691 tracking the Gulf Stream – North Atlantic Current advective pathway from the Caribbean to the
 692 subpolar latitudes. This *long memory* of past sea surface fluxes motivates the use of AMOC sensitivity to
 693 SST and SSS instead.



694

695 **Figure ED5.** North Atlantic mixed layer depth and spatial origins of buoyancy-
 696 **driven variability in RAPID-MOCHA overturning.** (a) Climatological March mixed
 697 layer depth [m] in ECCO; (b-e) Spatial sources of variability in the RAPID-MOCHA
 698 AMOC overturning: root-mean-square contribution per unit area [Sv m^{-2}] to the
 699 convolutions in equation (1) of the main text over the period 1992-2015 using
 700 sensitivity patterns based on (b,c) 2006-2007 and (d,e) 2001-2002 AMOC objective
 701 functions. Contributions due to SST (b,d), and SSS (c,e) all relative to the seasonal
 702 cycle. The scale in all panels is linear.